ADVANCED MATERIALS
www.advmat.de

# Strain Modulation for Light-Stable n–i–p Perovskite/Silicon Tandem Solar Cells

*Lina Wang, Qizhen Song, Fengtao Pei, Yihua Chen,* Jie Dou, Hao Wang, Congbo Shi, Xiao Zhang, Rundong Fan, Wentao Zhou, Zhiwen Qiu, Jiaqian Kang, Xueyun Wang, Andreas Lambertz, Mengru Sun, Xiuxiu Niu, Yue Ma, Cheng Zhu, Huanping Zhou, Jiawang Hong, Yang Bai, Weiyuan Duan,* Kaining Ding, and Qi Chen**

**Perovskite/silicon tandem solar cells are promising to penetrate photovoltaic market. However, the wide-bandgap perovskite absorbers used in top-cell often suffer severe phase segregation under illumination, which restricts the operation lifetime of tandem solar cells. Here, a strain modulation strategy to fabricate light-stable perovskite/silicon tandem solar cells is reported. By employing adenosine triphosphate, the residual tensile strain in the wide-bandgap perovskite absorber is successfully converted to compressive strain, which mitigates light-induced ion migration and phase segregation. Based on the wide-bandgap perovskite with compressive strain, single-junction solar cells with the n–i–p layout yield a power conversion efficiency (PCE) of 20.53% with the smallest voltage deficits of 440 mV. These cells also maintain 83.60% of initial PCE after 2500 h operation at the maximum power point. Finally, these top cells are integrated with silicon bottom cells in a monolithic tandem device, which achieves a PCE of 26.95% and improved light stability at open-circuit.**

## 1. Introduction

Hybrid halide perovskite is an excellent candidate for top cells in tandem solar cells due to its strong optical absorption, long diffusion lengths, and tunable bandgap.[1,2] Recently, tremendous efforts are reported to improve the efficiency of perovskite/silicon tandem solar cells, including composition tuning,[3] device structure design,[4,5] processing optimization,[6] light management,[7–9] and recombination layer optimization.[10] Currently, the certified power conversion efficiency (PCE) of 29.8% is achieved,[11] which have surpassed that of single-junction perovskite solar cells (25.7%) and market-dominant crystalline silicon photovoltaics (26.7%).[12]

To obtain wide-bandgap perovskites for top-cell, bromine (Br) and Cesium (Cs) are often alloyed in formamidinium lead iodide ($FAPbI_3$) to achieve a bandgap of 1.60–1.75 eV. Unfortunately, the migration of halide ions leads to significant phase segregation to form I-rich and Br-rich domains under continuous illumination. The phase segregation not only leads to large open-circuit voltage ($V_{OC}$) deficit due to I-rich domains,[13,14] but also gives birth to extra nonradiative-recombination centers to deteriorate the device power output.[15] The device lifetime is thus hampered, which limits the commercialization of perovskite/silicon tandem solar cells.

To solve the problem, many strategies have been explored recently. First, composition engineering can improve the

L. Wang, Q. Song, F. Pei, Y. Chen, J. Dou, H. Wang, C. Shi, X. Zhang, M. Sun, X. Niu, Y. Ma, C. Zhu, Y. Bai, Q. Chen
Experimental Center of Advanced Materials
School of Materials Science and Engineering
Beijing Institute of Technology
Beijing 100081, China
E-mail: yhchen@bit.edu.cn; qic@bit.edu.cn

The ORCID identification number(s) for the author(s) of this article can be found under https://doi.org/10.1002/adma.202201315.



**DOI: 10.1002/adma.202201315**

F. Pei, R. Fan, W. Zhou, Z. Qiu, H. Zhou
Beijing Key Laboratory for Theory and Technology of Advanced Battery Materials
Key Laboratory of Polymer Chemistry and Physics of Ministry of Education
BIC-ESAT
Department of Materials Science and Engineering
College of Materials Science and Engineering
Peking University
Beijing 100871, China

J. Kang, X. Wang, J. Hong
School of Aerospace Engineering
Beijing Institute of Technology
Beijing 100081, China

A. Lambertz, W. Duan, K. Ding
IEK-5 Photovoltaik
Forschungszentrum Jülich GmbH
52428 Jülich, Germany
E-mail: w.duan@fz-juelich.de

perovskite quality by A-site engineering and X-site cascade.[16–18] Second, additive engineering can optimize film morphology and passivate defects in the bulk and at the surface.[19] In addition, interface engineering, like 2D/3D heterostructures,[20] graded perovskite surface,[21] and so on, are reported to adjust band alignment and suppress the nonradiative recombination at the surface.[3,13,19,22]

Alternatively, residual strain are found to impact perovskite crystallinity, crystal phase stability, electronic band structure, and carrier dynamics within the device, which originates from their fabrication conditions including the material composition,[23] the substrate for film growth,[24] and external stimuli[25] during processing.[26] Moreover, residual strain correlates to I/Br phase segregation in wide-bandgap perovskite.[26–29] Recently, it is reported local tensile strain can facilitate light-induced phase segregation at grain boundaries and generate I-rich domains in I/Br alloyed perovskite films.[30] It is found that tensile strain results in weaken bonds to migration of halide ions.[23] The theoretical calculation demonstrates an increase activation energy for ion migration with compressive strain,[31] which is in accordance with experimental results.[32]

To date, strain engineering has been broadly studied in single-junction perovskite solar cells, which is seldom reported in perovskite/silicon tandem device. In this work, we first studied the relationship between strain type and phase segregation in I/Br alloyed wide-bandgap perovskites. By adding adenosine triphosphate (ATP), we obtain perovskite absorber with compressive strain, which enhances the energy barrier for ion migration and restrains light-induced phase segregation for not only A-site, but also X-site. Based on the modified 1.65-eV absorber, the single-junction device achieved a PCE of 20.53%. The $V_{OC}$ achieved 1.21 V with a 0.44 V $V_{OC}$-deficit, which was one of the lowest $V_{OC}$ deficits at present. Importantly, the devices after strain modulation exhibited a remarkable long-term operational stability by maintaining 83.60% of initial PCE after 2500 h maximum power point (MPP) tracking. Finally, we combined the optimized perovskite top cells with silicon bottom cells to fabricate two-terminal tandem solar cells, yielding a PCE of 26.95%.

## 2. Results and Discussion

### 2.1. Chemical Interaction and Residual Microstrain

To match the current of sub-cells, perovskite/silicon tandem devices require the bandgap of the perovskite absorber to be in the range of ≈1.60 and ≈1.68 eV, when considering their actual operating temperature.[33] We thus fabricated the perovskite absorber of $Cs_{0.22}FA_{0.78}Pb(I_{0.85}Br_{0.15})_3$ alloyed with 5% $MAPbCl_3$. The bandgap of this perovskite film was determined by the Tauc plot from the ultraviolet–visible (UV–vis) spectra, as shown in Figure S1, Supporting Information. Moreover, we introduced a foreign molecule ATP in perovskite absorber during film growth (see Supporting Information for details). Two kinds of perovskite films and corresponding cells fabricated with or without ATP molecule were denoted as REF and ATP, respectively.

As the molecular structure shown in **Figure 1**A, ATP molecule is composed of adenine, ribose and phosphate groups. We probed the chemical interaction between perovskite and ATP molecule by Fourier transform infrared spectroscopy (FTIR).

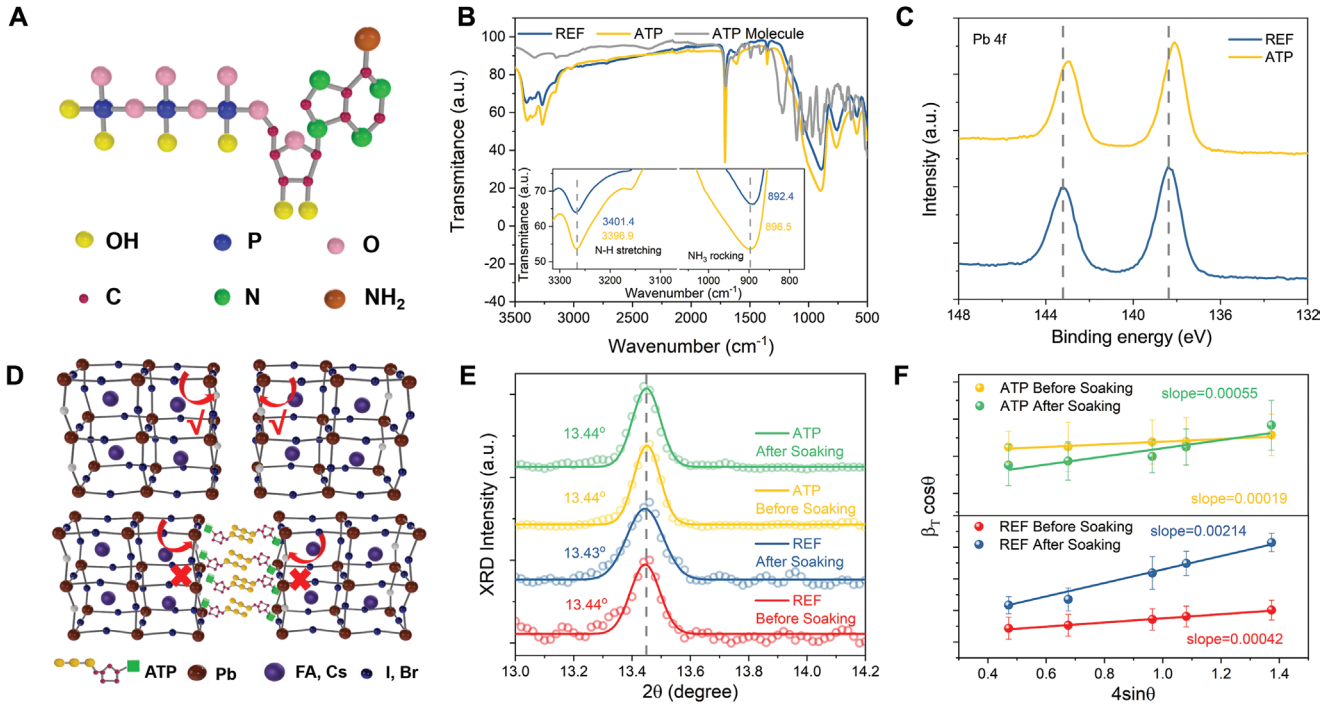


**Figure 1.** A) The structure of ATP molecule. B) FTIR spectra of REF and ATP films. C) XPS spectra of Pb 4f signal for REF and ATP films. D) The schematic describing of interaction between ATP and perovskite. E) XRD spectra in (001) planes of REF and ATP films before and after light soaking for 2 h. F) The W–H analysis for REF and ATP films before and after light soaking.

As shown in Figure 1B, the signals at 3401.4 and 892.4 $cm^{-1}$ are assigned to the stretching vibration of N—H and rocking vibration of $NH_3$ for A-site cation in hybrid perovskite, respectively.[34,35] When ATP was introduced, the signals shifted to 3396.9 and 896.5 $cm^{-1}$ for the stretch vibration of N—H and rock vibration of $NH_3$, respectively, suggesting the intermolecular hydrogen bonding between FA cation and ATP molecule.[34,35] Furthermore, we analyzed the chemical environment of various components in perovskites by X-ray photoelectron spectroscopy (XPS). As profiled in Figure 1C, the core level peaks of Pb 4f 7/2 and 4f 5/2 shifted to lower binding energies in ATP films, as compared with REF films, which means that $Pb^{2+}$ directly interacted with ATP molecule. Meanwhile, the negligible shift for peaks in XPS spectra of I, Br, and Cs were observed and summarized in Figure S2, Supporting Information. Thus, ATP molecule interacted with perovskites by hydrogen bonding with organic cations and coordination with $Pb^{2+}$.

Besides, we clearly observed P signals from the surface of perovskite films via XPS measurement, indicating the existence of ATP molecule at the surface possibly due to large steric hindrance of adenine and phosphate groups. In order to confirm the distribution of ATP molecule experimentally, we selected the P atom in ATP to study its distribution in perovskites by time of flight secondary ion mass spectrometry (ToF-SIMS) mapping. As shown in Figure S3, Supporting Information, we found that there was nearly no P signal in REF bulk, while it was obvious in ATP sample.[3] To further investigate the distribution of ATP molecules, we selected the areas of 500 nm × 500 nm to perform nano-FTIR analysis which simultaneously reconstructing atomic force microscopy (AFM) topography and broadband IR response of surfaces,[36] as shown in Figure S4, Supporting Information. We adopted the P—O characteristic vibrational mode[37] at 1241 $cm^{-1}$ to track the existence of ATP molecules. Interestingly, these characteristic IR signals were mostly observed at the grain boundaries, while there were nearly no signals within the grains, which clearly illustrates the ATP molecules prefer to stay at the grain boundaries. The schematic diagram was illustrated in Figure 1D. In addition, we discussed the impact of ATP on the grain size or morphology of perovskite film, as shown in Note S1, Supporting Information.

We find ATP molecules could affect the residual local strain in polycrystalline films, which further impacts the ion migration and phase segregation in perovskites. X-ray diffraction (XRD) was employed to analyze the crystal structural change of perovskite films upon illumination. REF and ATP films were both exposed under continuous illumination of simulated sunlight (xenon lamp, AM 1.5G, one sun, 100 mW $cm^{-2}$, 50 °C) for 2 h to accelerate their ion migration and phase segregation. All XRD spectra for REF and ATP films before and after light ageing were shown in Figure S5, Supporting Information. It shows distinct diffraction peaks at ≈13.5°, 31.4°, and 40.2°, corresponding to crystallographic planes of (100), (012), and (022), respectively.[38] We picked the characteristic peak at ≈13.5° to observe that it was broadened and slightly shifted to the lower diffraction angle in the REF film after light ageing as shown in Figure 1E. It is possible that iodine-rich segregations with larger lattice constant were formed in aged REF films, which is in line with pervious observation.[39] Surprisingly, there was no obvious shift and widen for (100) peak in ATP films after ageing.

Subsequently, we estimated the microstrain within the films by using Williamson–Hall (W–H) method to in-depth understand the variation of XRD peaks (see Supporting Information for details). As shown in Figure 1F, before continuous light ageing, both REF and ATP films exhibited microstrain, wherein the slope of the fitted curves are found to be 0.00042 and 0.00019, respectively. It indicates that the microstrain in REF films is larger than that in ATP films during the preparation. After light ageing, the REF films have significantly larger microstrain than that in the ATP films, revealing that ATP molecules could achieve the smaller microstrain in both preparation and ageing stages.[40,41]

### 2.2. Strain Modulation Restricts Ionic Migration

We find ATP additives can modulate macro strain types of resultant perovskite films. We conducted grazing incident XRD (GIXRD) measurement on the absorber films with the probe depth of ≈500 nm, which were deposited on the top of silicon cells (Supporting Information). And we chose the characteristic peak at ≈31.4°, corresponding to (012) plane, to conduct further analysis with the most reliable structural symmetry information.[23] As shown in **Figure 2**A, it was obvious that the position of characteristic peak gradually shifted to a lower diffraction degree with the instrument tilt angles $\psi$ varies from 0° to 50°, suggesting the increasing of crystal plane distance $d_{(012)}$ for REF films. The results clearly indicated that the REF film was bearing a large in-plane tensile strain as a whole. On the contrary, the characteristic peaks for ATP films showed a clear movement to a higher diffraction degree by varying the instrument tilt angles $\psi$ from 0° to 50°, which demonstrated the reduced crystal plane distance $d_{(012)}$, as presented in Figure 2B. Moreover, we fit the diffraction data ($2\theta$) with Gaussian distribution function, and then profiled the linear relationship between $2\theta$ and $\sin^2\psi$, as shown in Figure 2C. The fitting lines exhibited a negative slope for REF films and a positive slope for ATP films, and the tensile stress value was estimated as 16 ± 1 MPa in REF films while the compressive stress value in ATP films was estimated as 13 ± 1 MPa, respectively. This distinct difference indicates that ATP molecule could modify the strain status of perovskite absorber on silicon bottom cells from tensile to compressive strain. In addition, we also studied the macro strain types for both REF and ATP films deposited on the glass/ITO/$SnO_2$ substrates. As shown in Figure 2D and Figure S6, Supporting Information, similar change from tensile to compressive strain was observed, when ATP was introduced in the films. By linear fitting $2\theta$ with $\sin^2\psi$, we also estimated that the tensile stress value was 43 ± 1 MPa in REF film and the compressive stress value was 42 ± 3 MPa in ATP film on glass substrates. Similarly, ATP molecule spin coated at the surface (top and bottom) could achieve in-plane compressive strain (see Note S2, Supporting Information). We speculate the compressive stress is possibly attributed to ATP at the grain boundaries and surface, which would squeeze crystal lattice during annealing.[24,29,42] In order to insure the reproducibility of result, we reconducted GIXRD measurement, demonstrating the same result as shown in Figure S7, Supporting Information and Table S1, Supporting Information. In addition, ATP films with compressive strain

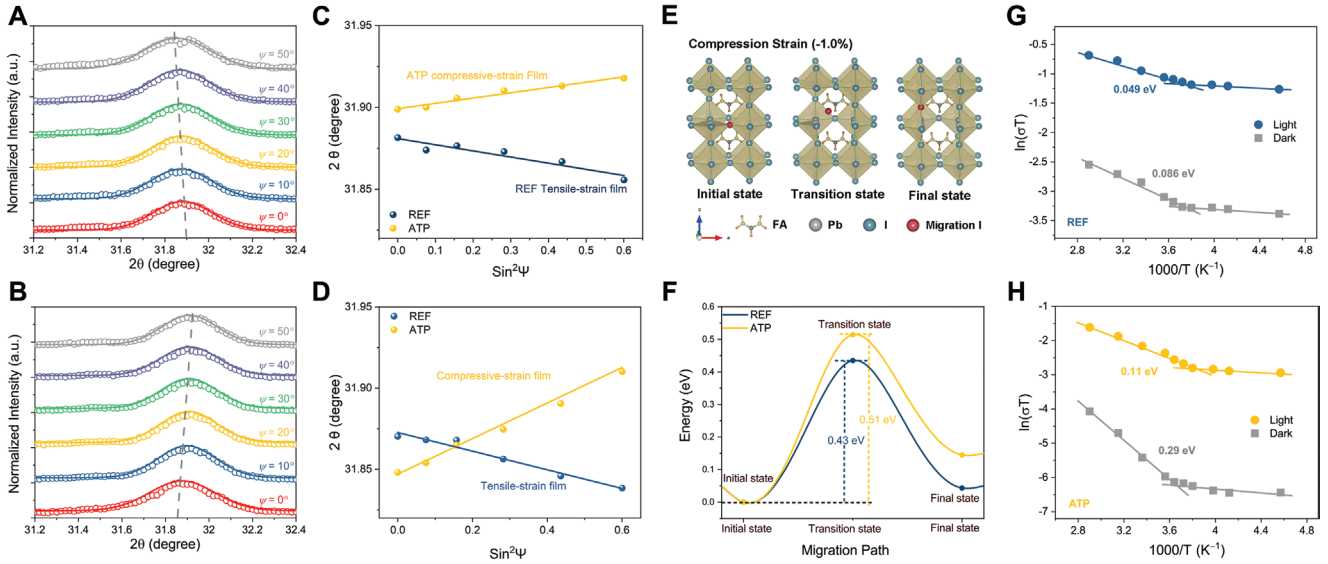


**Figure 2.** A,B) Different instrumental $\psi$ values in XRD for REF (A) and ATP (B) films (hollow circles, measured XRD patterns; solid lines, the fitted results with the Gauss function) at a depth of 500 nm, respectively, which are deposited on the top of silicon cells. C,D) Linear fit of $2\theta$-$\sin^2\psi$ at a depth of 500 nm for ATP and REF films on $SnO_2$/silicon substrate (C) and $SnO_2$/glass cells substrate (D). E) Scheme of ion migration under compressive strain in the DFT calculation. F) Strain-dependent activation energies for the vacancy-assisted migration of halide ions for REF and ATP films from DFT calculation. G,H) The temperature-dependent conductivity for REF (G) and ATP (H) films under dark and light conditions.

exhibited valence band (VB) upshifting from the ultraviolet photoelectron spectroscopy (UPS) results as shown in Figure S8, Supporting Information. This result further confirmed the compressive strain in ATP films, agreeing with past reports.[23] We thus achieved effective strain modulation by ATP molecule in both I/Br alloyed wide-bandgap perovskite solar cells and corresponding tandem devices.

We further studied how macro strain impact ion migration through density functional theory (DFT) calculation. Both tensile and compressive strains were simulated by applying different ratio of biaxial strain from +1.0% to −1.0%. We investigated the possible route of ion migration and the activation energy ($E_a$) in different films. The details are presented in Supporting Information. Figure 2E displays the migration route for I ion between two adjacent sites in ATP and REF films, from which we estimate the corresponding $E_a$ of REF and ATP films. When the tensile strain in perovskites was converted to compressive strain, the $E_a$ for ion migration was improved from 0.43 to 0.51 eV (Figure 2F). This result illustrates that compressive strain in ATP films could increase barrier for ion migration.

Furthermore, we measured the temperature-dependent conductivity of REF and ATP films under dark and light conditions. The experimental activation energies ($E_{a.e}$) for ion migration were extracted following Nernst–Einstein equation (Supporting Information). As shown in Figure 2G,H, for REF films with tensile strain, the $E_{a.e}$s of ion migration in dark and light conditions were 0.086 and 0.049 eV, respectively. When the tensile strain was converted to compressive strain by ATP molecule, the $E_{a.e}$s in dark and light conditions were increased to 0.29 and 0.11 eV, respectively. These results are consistent with the previous simulation, and further underline the effectively suppressed ion migration in perovskite absorber by strain modulation.

### 2.3. Strain Modulation Suppresses Phase Segregation

It's well known that restricting ion migration helps to suppress light-induced phase segregation in perovskites.[43] To visualize the impact of strain modulation by ATP molecule on the evolution of perovskite phase under illumination, the time-dependent Photoluminescence (PL) measurement was applied. The emission spectra of REF and ATP films were recorded, immediately after fixed periods of light exposure by one-sun equivalent white LED. As shown in **Figure 3**A,B, REF and ATP films both exhibited an emission peak at ≈750 nm before light soaking (0 min). Along with the increase of illumination time, the emission peak of REF gradually redshifted. After 20 min illumination, an obvious redshift of ≈761 nm was observed for REF films. In contrast, there was no detectable variation for ATP films in the first 30 min ageing, and it showed a slight redshift until 45 min. Finally, the emission of REF films shifted to ≈773 nm while that of ATP films nearly kept at ≈762 nm, after 90 min light soaking. The obvious redshift of peaks was mainly contributed to I-rich domain formed under illumination.[14] This result indicates that the strain modulation by ATP molecule effectively suppress light-induced phase segregation and offer a superior photostability.

Moreover, we further conducted the ex-situ 2D PL mapping for both REF and ATP films under illumination of simulated sunlight by a xenon lamp (AM 1.5G, one sun, 100 mW cm$^{-2}$, 50 °C). As shown in Figure 3C, the characteristic emission of REF and ATP films were similar and homogeneous at initial state (0 min). After light soaking of 60 min, the REF film exhibited obvious PL redshift and wavelength heterogeneity. After 120 min light soaking, we observed the significant redshifted emission occurred in almost all measured area of REF films. In contrast, the PL heterogeneity was mitigated in ATP films.

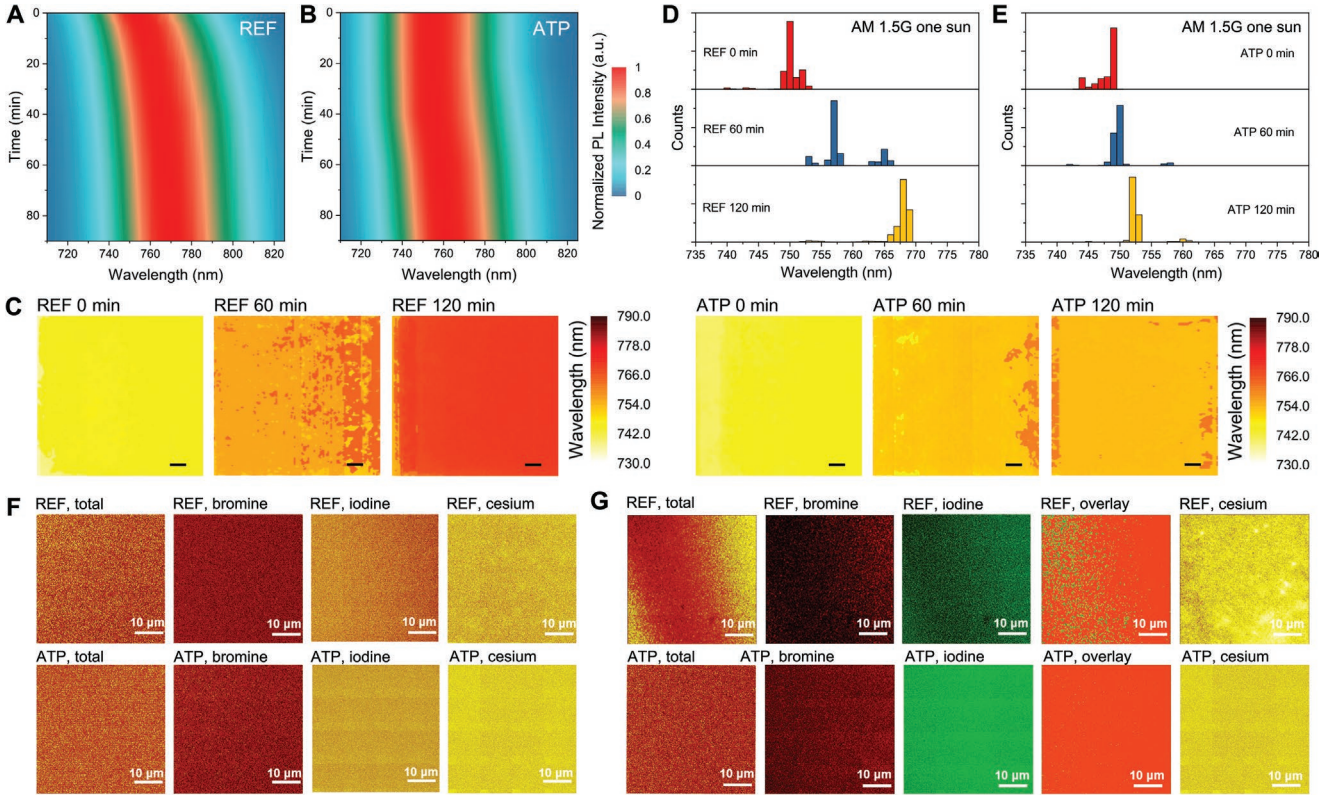


**Figure 3.** A,B) Evolution of PL spectra for REF (A) and ATP (B) films under one-sun equivalent white LED illumination over 1.5 h. C) The PL mapping of REF and ATP films under one-sun illumination (AM 1.5G, 100 mW cm$^{-2}$) for 2 h; scale bar: 10 μm. D,E) PL mapping emission peak statistical diagram of REF films (D) and ATP films (E). F,G) ToF-SIMS mapping of REF and ATP films, including total ion, Br ion, I ion, I–Br overlay, and Cs ion before light soaking (F) and after light soaking (G).

We further quantify the wavelength variations across the entire PL regions to assess the extent of phase segregation. Before the light ageing (0 min), almost all emission peaks were both centered at ≈748 nm for REF and ATP film. After light exposure for 60 min, REF films exhibited a slight splitting of the emission peak, and two extra emission peaks were concentrated at ≈757 and ≈765 nm (Figure 3D), which was not found in ATP films at the same ageing condition. Besides, with the ageing time prolonged to 120 min, the centered wavelength of emission peak shifted from ≈748 to ≈768 nm due to the dominating emission of iodine-rich segregation in REF. Interestingly, the ATP films exhibited just a slight redshift from ≈748 to ≈752 nm in the statistics profile (Figure 3E), suggesting almost suppressed phase segregation. The peak distributions in 2D PL mapping evolved as consistent with the time-dependent PL spectra (Figure 3A,B). Moreover, the in-situ PL mappings for both REF and ATP films under illumination of 457 nm laser (15 mW cm$^{-2}$, 300 K) were recorded (Figure S9, Supporting Information). Due to the large intensity of the laser probe, the PL mapping revealed a small circular plot after 5 min illumination, in which the light-induced phase segregation occurred. Along with the increase of illumination time, the circular plot gradually enlarged for REF films. In contrast, the light-induced phase segregation was suppressed in ATP films, as also evidenced by the peak statistics in entire measured regions (Figure S10, Supporting Information). In addition, the time-dependent UV–vis spectroscopy also reveals that the compressive strain helps to prevent the redshift of the bandgap due to the phase segregation in wide-bandgap perovskite, as compared with REF films (Figure S11, Supporting Information).

Beyond the emission mapping and bandgap analysis, we also performed 2D ToF-SIMS mapping to directly visualize the composition segregation due to ionic migration. As shown in Figure 3F, all ions of interest, including Br, I, and Cs ions, show homogeneous distribution in both REF and ATP films before the light ageing. After light ageing (AM 1.5G, one sun, 100 mW cm$^{-2}$, 50 °C) for 4 h, both Br distribution and I distribution of REF films in Figure 3G exhibited distinct segregation. We further overlaid the Br and I distributions to observe obvious domains at the scale of several micrometers. In contrast, ATP films after effective strain modulation showed superior homogeneity in both Br and I distributions, which was consistent with relatively uniform PL emission in previous experiment. To be noted, Cs distribution also showed an obvious segregation in REF films, while it was absent in ATP films. Although Cs heterogeneity has less effect on the bandgap of wide-bandgap perovskites than the Br/I phase segregation, it promotes the degradation of perovskite solar cells under illumination.[44] Thus, it's worth highlighting that the strain modulation here demonstrates universality in inhibiting various ion migration and mitigating different phase segregation, which ensures the great operation stability or photostability of wide-bandgap perovskite based solar cells.

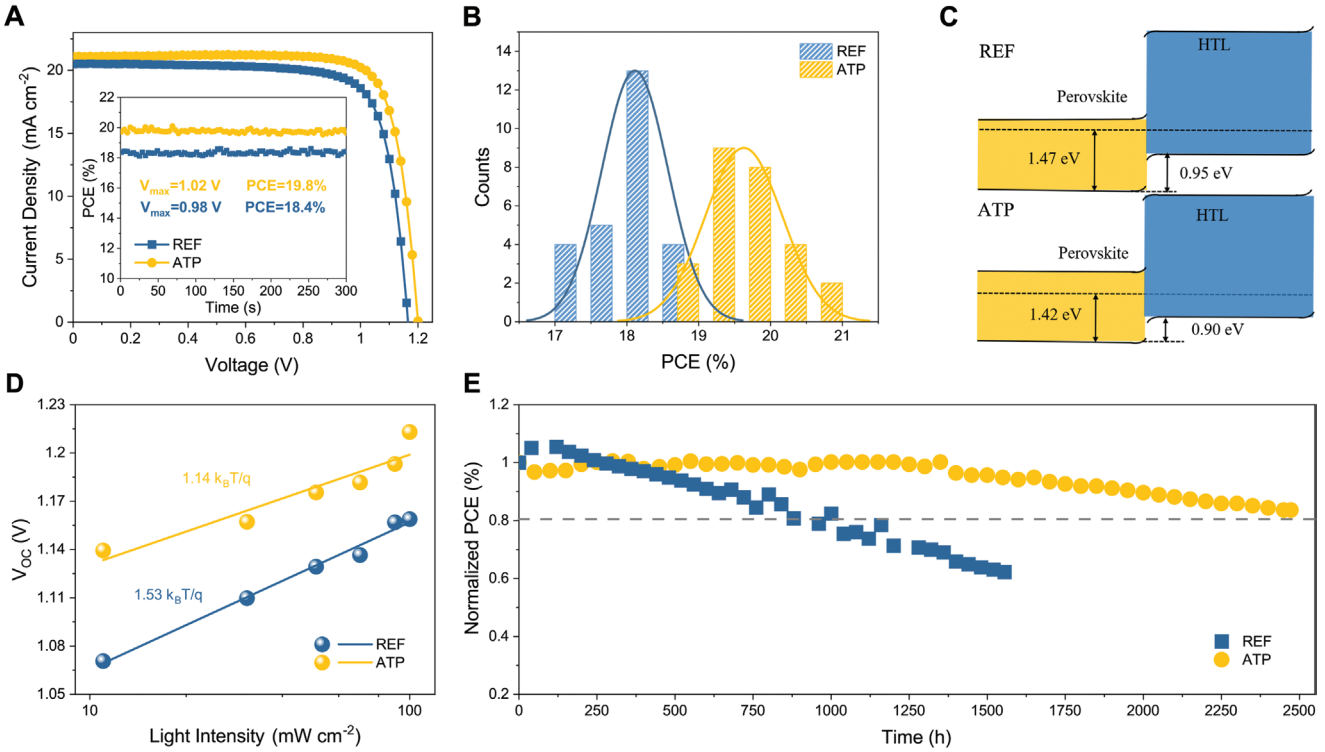


**Figure 4.** A) *J–V* curves of REF and ATP devices. The inset is the stabilized PCE measured at a bias voltage (0.98 V for REF devices and 1.02 V for ATP devices, respectively). B) A histogram of the PCEs for REF and ATP devices. C) Bandgap diagram between perovskite and Spiro-OMeTAD from UPS results. D) The light-intensity dependence of $V_{OC}$ measurement related to REF and ATP devices. E) The long-term continuous MPP tracking for REF and ATP devices using white LED with a light intensity of 100 mW cm$^{-2}$.

### 2.4. Performance of Single-Junction Perovskite Solar Cells

Strain modulation not only leads to the restricted light-induced ion migration and phase segregation in perovskites, but also improves the optoelectronic properties of perovskite films and thus devices. We conducted the time-resolved PL and PL measurements to investigate carrier recombination in both REF and ATP films with a structure of glass/perovskite. As shown in Figure S12, Supporting Information, the improved carrier lifetime and emission intensity suggested decreased defect density, which also reduced the routes for ion migration in resulted ATP films.

Subsequently, we prepared the planar n–i–p perovskite solar cells to study the influence of strain modulation on its photovoltaic performance. The optimal concentration of ATP was found to be 0.25 mg mL$^{-1}$ (Figure S13, Note S3, Supporting Information). And we achieved the champion PCE of 20.53% with the active area of 0.0805 cm$^2$. It exhibited a $V_{OC}$ of 1.21 V, a short-circuit current density ($J_{SC}$) of 21.08 mA cm$^{-2}$ and a fill factor (FF) of 80.49% in ATP devices, while the REF devices showed a PCE of 18.59%, as shown in **Figure** 4A. The superior $V_{OC}$ ensured a low deficit of 440 mV, which was one of the lowest $V_{OC}$-deficits in I/Br alloyed wide-bandgap perovskite solar cells with n–i–p structure. Besides, the champion device gave a stabilized power output (SPO) of 19.8% by holding a bias near the maximum power output point (1.02 V), as shown in the inset of Figure 4A. Moreover, we further conducted the statistical analysis on 27 individual devices in each group. As shown in Figure 4B, the histogram indicated the great reproducibility and verified the PCE enhancement from 18.1 ± 0.8% to 19.8 ± 1.1% by strain modulation. And corresponding statistics of $V_{OC}$, $J_{SC}$ and FF were shown in Figure S14, Supporting Information. The average $V_{OC}$ increased by 50 mV from 1.15 ± 0.02 V to 1.20 ± 0.01 V, which was caused by reduced nonradiative recombination. The average FF increased from 73 ± 3% to 79 ± 3%, and the average $J_{SC}$ improved from 20.3 ± 0.5 to 21.0 ± 0.4 mA cm$^{-2}$, mainly due to better carrier transport by strain modulation.

As shown in Figure 4C and Figure S8, Supporting Information, we found that the VB edge showed a downshift due to the weakening Pb—X bonds under tensile strain in REF films, however, it upshifted for ATP films because of the strengthening Pb—X bonds under compressive strain.[23] The optimized band alignment between perovskite and Spiro-OMeTAD was responsible for the increased $J_{SC}$, which was consistent with the integrated current density by the external quantum efficiency (EQE), as shown in Figure S15, Supporting Information. At the same time, we confirmed the bandgap of the perovskite devices of 1.65 eV from EQE measurements. Finally, we studied the internal recombination mechanism of REF and ATP devices by sun-dependent $V_{OC}$. As shown in Figure 4D, the ideality factors were calculated as 1.14 and 1.53 for ATP and REF devices, respectively, which indicated that the defect-assisted SRH recombination in wide-bandgap perovskite solar cells was effectively suppressed. In order to further investigate how strain impacts defect density, carrier recombination and transport, we

conducted the space-charge-limited current analysis, transient photovoltage decay, and transient photocurrent decay measurements, as shown in Note S4, Supporting Information.

In order to assess the influence of strain modulation on photostability of wide-bandgap perovskite solar cells, we monitored the long-term SPO of unencapsulated devices at one-sun LED illumination in a nitrogen atmosphere by holding the applied bias at maximum power point. Here, we adopted perovskite solar cells with the structure of planer p-i-n inverted configuration to avoid the influence of aged Spiro-OMeTAD (see details in Note S5, Supporting Information). As shown in Figure 4E, the ATP devices with strain modulation maintained 83.60% of their initial PCE after 2500 h, while the REF devices dropped to 62.20% after 1500 h. Besides, we also studied the long-term photostability of unencapsulated devices under open-circuit condition at same illumination. As shown in Figure S16, Supporting Information, the ATP devices kept 77.93% of their initial PCE after 1500 h irradiation, while the REF cells maintained 52.66% after 1000 h. The prolonged lifetimes manifested that strain modulation in perovskite absorber effectively restricts light-induced phase segregation, which significantly extends the operational lifetime of the corresponding devices.

### 2.5. Performance of Perovskite/Silicon Tandem Solar Cells

Strain modulation has shown the superior in both PCE and stability for perovskite single junctions, which could be transfered into monolithic tandem devices. We integrated the monolithic perovskite/silicon tandem solar cells with n–i–p structured wide-bandgap perovskite top cells and single-side textured silicon heterojunction (SHJ) bottom cells. After cutting into the appropriate size, the adopted SHJ bottom cells were measured to exhibit a PCE of 20.1%, with a $V_{OC}$ of 0.71 V, a $J_{SC}$ of 34.9 mA cm$^{-2}$ and an FF of 80.95% (Figure S17, Supporting Information). The scheme and cross-section SEM image were shown in **Figure 5**A. Different from single-junction cells, 5 nm of MoOx was deposited by thermal evaporation in tandem devices to avoid the damage from sputtering ITO. And the designed top grid pattern was shown in Figure S18, Supporting Information. In addition, the mixed hole transport layer (Spiro-OMeTAD and PTAA) was applied to minimize the parasitic absorption of doped Spiro-OMeTAD in the range of 300–430 nm to improve the photovoltaic performance of tandem device,[45] as shown in Figures S19, S20, Supporting Information.

Subsequently, we measured the *J–V* curves of monolithic tandem devices and attained a champion PCE of 26.95% under reverse scan, with a $V_{OC}$ of 1.85 V, a $J_{SC}$ of 18.04 mA cm$^{-2}$ and an FF of 80.76% for ATP based tandem devices. Correspondingly, *J–V* curve under forward scan indicated a PCE of 26.01%, with a $V_{OC}$ of 1.82 V, a $J_{SC}$ of 17.91 mA cm$^{-2}$ and an FF of 79.80%, as summarized in Figure 5B. Besides, we further monitored the SPO of REF and ATP tandem devices by holding the applied voltage near maximum power point (1.60 and 1.54 V), respectively (Figure 5C). The ATP tandem devices gave a higher stabilized PCE of 26.0% than 24.8% of REF tandem devices, in line with the photovoltaic performance of single-junction counterparts. Figure 5D shows the EQE response of champion tandem device. The integrated current density in perovskite

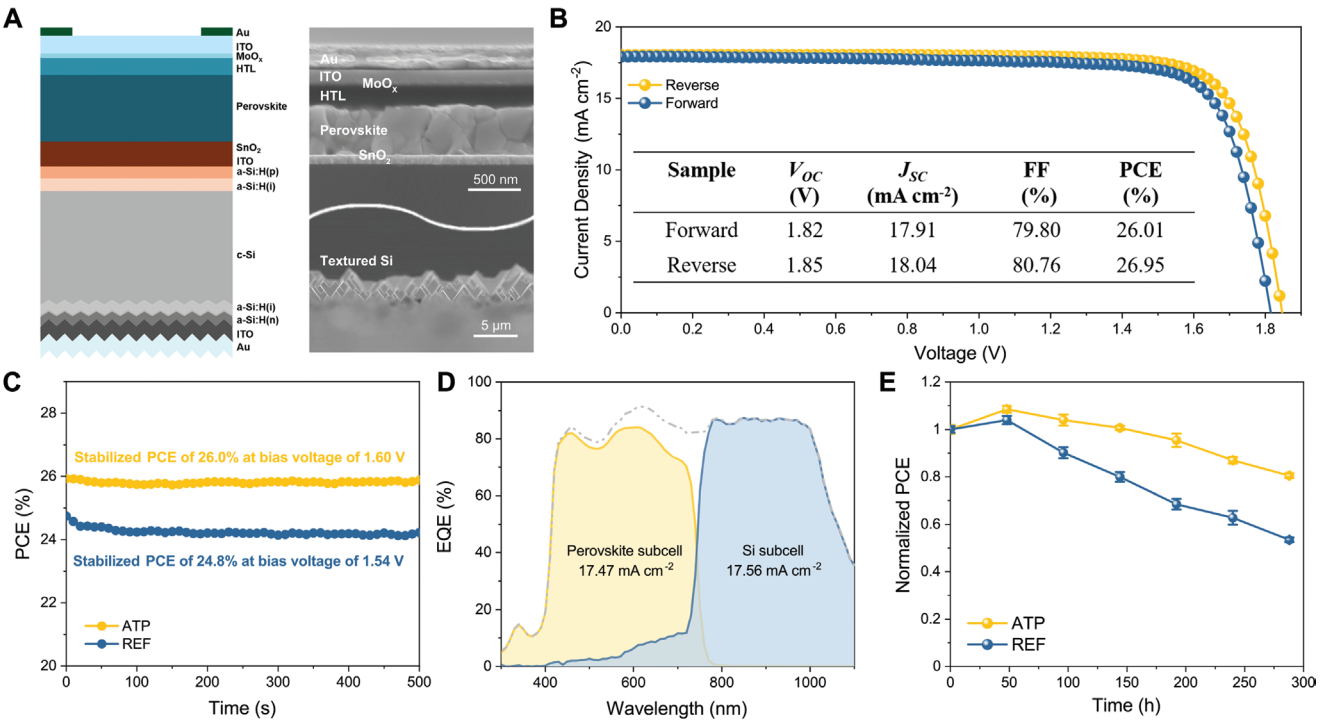


**Figure 5.** A) Schematic stack and cross-section SEM image of perovskite/silicon tandem solar cells. B) *J–V* curves of ATP tandem devices. C) The SPO measured at bias voltages of 1.60 V for ATP tandem devices and 1.54 V for REF tandem devices. D) EQE spectra measured in the champion perovskite/silicon tandem solar cells. E) The photostability of REF and ATP tandem devices.

and silicon subcells were 17.43 and 17.52 mA $cm^{-2}$, respectively, which was in excellent agreement with that derived from *J–V* curves.

We further tracked the long-term stability of REF and ATP tandem devices to confirm the impact of strain modulation. The unencapsulated devices were aged under one sun-equivalent LED in a nitrogen atmosphere, and the *J–V* curves were recorded for every 50 h. As shown in Figure 5E, after 300 h, the ATP tandem devices maintained 80.50% of their initial PCE, while the REF tandem devices just retained 53.45%. The improved photostability in tandem devices was originated from the suppressed light-induced phase segregation in perovskite absorbers.

## 3. Conclusion

We have investigated the influence of residual strain on phase segregation in perovskite/silicon tandem solar cells for the first time. The tensile strain in I/Br alloyed wide-bandgap perovskites is effectively converted to compressive strain by ATP incorporation in the film, which significantly retards both A-site and X-site segregation. In addition, strain modulation results in improved carrier transport at the interface and less defect density in the perovskite film, which mitigates ion migration. In wide-bandgap solar cells with compressive strain, we acquire an increased PCE of 20.53% with lower $V_{OC}$ deficit of 440 mV, which is one of the lowest $V_{OC}$ deficits. The unencapsulated device remains 83.60% of its initial efficiency after 2500 h of MPP tracing under one sun-equivalent white LED illumination. Furthermore, we fabricated the monolithic perovskite/silicon tandem solar cells with n–i–p architecture and achieved a PCE of 26.95% and prolonged lifetime with compressive strain. Our findings provide an alternative approach to suppress light-induced phase segregation by strain modulation, which guides the development of highly light-stable wide-bandgap perovskite and tandem devices.

## Supporting Information

Supporting Information is available from the Wiley Online Library or from the author.

## Acknowledgements

This work was supported by the National Natural Science Foundation of China (Grant nos. 21975028, 51972004, 22005035), National Key Research and Development Program of China (Grant nos. 2017YFA0206701, 2020YFB1506400), the Federal ministry of Economic Affairs and Energy in the framework of the STREET project (Grant no. 0324275E), TOUCH project (Grant no. 0324351), the Helmholtz Energy Materials Foundry (HEMF) infrastructure funded by the HGF. The authors also thank the China Postdoctoral Science Foundation (Grant no. 2021M700400) for the support.

Open access funding enabled and organized by Projekt DEAL.

## Conflict of Interest

The authors declare no conflict of interest.

## Author Contributions

L.W., Y.C., and Q.C. conceived and supervised the project. L.W. fabricated and characterized the films and devices and performed the stability test. Z.Q. and F.P. assisted in device fabricating. Q.S. performed the DFT calculation. W.D., A.L., and K.D. processed and optimized the SHJ bottom cells. W.Z., Y.M., R.F., and F.P. assisted in characterization. C.S., X.N. conceived the molecular discussion. J.D. performed the SEM measurements. H.W. and C.Z. performed the GIXRD measurements. X.Z. performed the PL mapping measurements. J.K., X.W., and J.H. performed AFM measurement. M.S. assisted in drawing schematic diagram. Y.B. performed the ToF-SIMS measurements. L.W. wrote the first draft of the manuscript. L.W., Y.C., H.Z. W.D., and Q.C. revised the manuscript. All authors contributed to the discussion and commented on the manuscript.

## Data Availability Statement

The data that support the findings of this study are available from the corresponding author upon reasonable request.

## Keywords

open-circuit voltage, perovskite/silicon tandem solar cells, phase segregation, strain modulation

Received: February 9, 2022
Revised: March 23, 2022
Published online: May 17, 2022

[1] H. Zhou, Q. Chen, G. Li, S. Luo, T. B. Song, H. S. Duan, Z. Hong, J. You, Y. Liu, Y. Yang, *Science* **2014**, *345*, 542.
[2] N. Li, X. Niu, L. Li, H. Wang, Z. Huang, Y. Zhang, Y. Chen, X. Zhang, C. Zhu, H. Zai, Y. Bai, S. Ma, H. Liu, X. Liu, Z. Guo, G. Liu, R. Fan, H. Chen, J. Wang, Y. Lun, X. Wang, J. Hong, H. Xie, D. S. Jakob, X. G. Xu, Q. Chen, H. Zhou, *Science* **2021**, *373*, 561.
[3] T. C.-J. Yang, P. Fiala, Q. Jeangros, C. Ballif, *Joule* **2018**, *2*, 1421.
[4] Z. Song, C. Chen, C. Li, R. A. Awni, D. Zhao, Y. Yan, *Semicond. Sci. Technol.* **2019**, *34*, 093001.
[5] G. E. Eperon, M. T. Hörantner, H. J. Snaith, *Nat. Rev. Chem.* **2017**, *1*, 0095.
[6] F. Sahli, J. Werner, B. A. Kamino, M. Brauninger, R. Monnard, B. Paviet-Salomon, L. Barraud, L. Ding, J. J. Diaz Leon, D. Sacchetto, G. Cattaneo, M. Despeisse, M. Boccard, S. Nicolay, Q. Jeangros, B. Niesen, C. Ballif, *Nat. Mater.* **2018**, *17*, 820.
[7] B. Chen, S.-W. Baek, Y. Hou, E. Aydin, M. De Bastiani, B. Scheffel, A. Proppe, Z. Huang, M. Wei, Y.-K. Wang, E.-H. Jung, T. G. Allen, E. Van Kerschaver, F. P. García de Arquer, M. I. Saidaminov, S. Hoogland, S. De Wolf, E. H. Sargent, *Nat. Commun.* **2020**, *11*, 1257.
[8] Z. Qiu, Z. Xu, N. Li, N. Zhou, Y. Chen, X. Wan, J. Liu, N. Li, X. Hao, P. Bi, Q. Chen, B. Cao, H. Zhou, *Nano Energy* **2018**, *53*, 798.
[9] L. Mazzarella, Y. H. Lin, S. Kirner, A. B. Morales-Vilches, L. Korte, S. Albrecht, E. Crossland, B. Stannowski, C. Case, H. J. Snaith, R. Schlatmann, *Adv. Energy Mater.* **2019**, *9*, 1803241.
[10] N. Liu, L. Wang, F. Xu, J. Wu, T. Song, Q. Chen, *Front. Chem.* **2020**, *8*, 603375.
[11] NREL, Best Research-Cell Efficiency Chart, https://www.nrel.gov/pv/cellefficiency.html (accessed: November 2021).
[12] K. Yoshikawa, H. Kawasaki, W. Yoshida, T. Irie, K. Konishi, K. Nakano, T. Uto, D. Adachi, M. Kanematsu, H. Uzu, K. Yamamoto, *Nano Energy* **2017**, *2*, 17032.

[13] D. Luo, R. Su, W. Zhang, Q. Gong, R. Zhu, *Nat. Rev. Mater.* **2020**, *5*, 44.
[14] E. L. Unger, L. Kegelmann, K. Suchan, D. Sörell, L. Korte, S. Albrecht, *J. Mater. Chem. A* **2017**, *5*, 11401.
[15] M. C. Brennan, S. Draguta, P. V. Kamat, M. Kuno, *ACS Energy Lett.* **2017**, *3*, 204.
[16] D. Kim, H. J. Jung, I. J. Park, B. W. Larson, S. P. Dunfield, C. Xiao, J. Kim, J. Tong, P. Boonmongkolras, S. G. Ji, F. Zhang, S. R. Pae, M. Kim, S. B. Kang, V. Dravid, J. J. Berry, J. Y. Kim, K. Zhu, D. H. Kim, B. Shin, *Science* **2020**, *368*, 155.
[17] K. A. Bush, K. Frohna, R. Prasanna, R. E. Beal, T. Leijtens, S. A. Swifter, M. D. McGehee, *ACS Energy Lett.* **2018**, *3*, 428.
[18] D. P. McMeekin, G. Sadoughi, W. Rehman, G. E. Eperon, M. Saliba, M. T. Horantner, A. Haghighirad, N. Sakai, L. Korte, B. Rech, M. B. Johnston, L. M. Herz, H. J. Snaith, *Science* **2016**, *351*, 151.
[19] J. Tong, Q. Jiang, F. Zhang, S. B. Kang, D. H. Kim, K. Zhu, *ACS Energy Lett.* **2020**, *6*, 232.
[20] J. J. Yoo, S. Wieghold, M. C. Sponseller, M. R. Chua, S. N. Bertram, N. T. P. Hartono, J. S. Tresback, E. C. Hansen, J.-P. Correa-Baena, V. Bulović, T. Buonassisi, S. S. Shin, M. G. Bawendi, *Energy Environ. Sci.* **2019**, *12*, 2192.
[21] D. Luo, W. Yang, Z. Wang, A. Sadhanala, Q. Hu, R. Su, R. Shivanna, G. F. Trindade, J. F. Watts, Z. Xu, T. Liu, K. Chen, F. Ye, P. Wu, L. Zhao, J. Wu, Y. Tu, Y. Zhang, X. Yang, W. Zhang, R. H. Friend, Q. Gong, H. J. Snaith, R. Zhu, *Science* **2018**, *360*, 1442.
[22] C. Geng, X. Chen, S. Li, Z. Ding, W. Ma, J. Qiu, Q. Wang, C. Yan, H.-j. Fan, *Energy Mater. Adv.* **2021**, *2021*, 8481915.
[23] C. Zhu, X. Niu, Y. Fu, N. Li, C. Hu, Y. Chen, X. He, G. Na, P. Liu, H. Zai, Y. Ge, Y. Lu, X. Ke, Y. Bai, S. Yang, P. Chen, Y. Li, M. Sui, L. Zhang, H. Zhou, Q. Chen, *Nat. Commun.* **2019**, *10*, 815.
[24] N. Rolston, K. A. Bush, A. D. Printz, A. Gold-Parker, Y. Ding, M. F. Toney, M. D. McGehee, R. H. Dauskardt, *Adv. Energy Mater.* **2018**, *8*, 1802139.
[25] B. Chen, T. Li, Q. Dong, E. Mosconi, J. Song, Z. Chen, Y. Deng, Y. Liu, S. Ducharme, A. Gruverman, F. Angelis, J. Huang, *Nat. Mater.* **2018**, *17*, 1020.
[26] H.-S. Kim, N.-G. Park, *NPG Asia Mater* **2020**, *12*, 78.
[27] E. G. Moloney, V. Yeddu, M. I. Saidaminov, *ACS Mater. Lett.* **2020**, *2*, 1495.
[28] D. Liu, D. Luo, A. N. Iqbal, K. W. P. Orr, T. A. S. Doherty, Z.-H. Lu, S. D. Stranks, W. Zhang, *Nat. Mater.* **2021**, *20*, 1337.
[29] H. Wang, C. Zhu, L. Liu, S. Ma, P. Liu, J. Wu, C. Shi, Q. Du, Y. Hao, S. Xiang, H. Chen, P. Chen, Y. Bai, H. Zhou, Y. Li, Q. Chen, *Adv. Mater.* **2019**, *31*, 1904408.
[30] Y. Zhao, P. Miao, J. Elia, H. Hu, X. Wang, T. Heumueller, Y. Hou, G. J. Matt, A. Osvet, Y. T. Chen, M. Tarrago, D. de Ligny, T. Przybilla, P. Denninger, J. Will, J. Zhang, X. Tang, N. Li, C. He, A. Pan, A. J. Meixner, E. Spiecker, D. Zhang, C. J. Brabec, *Nat. Commun.* **2020**, *11*, 6328.
[31] D. J. Xue, Y. Hou, S. C. Liu, M. Wei, B. Chen, Z. Huang, Z. Li, B. Sun, A. H. Proppe, Y. Dong, M. I. Saidaminov, S. O. Kelley, J. S. Hu, E. H. Sargent, *Nat. Commun.* **2020**, *11*, 1514.
[32] J. Zhao, Y. Deng, H. Wei, X. Zheng, Z. Yu, Y. Shao, J. E. Shield, J. Huang, *Sci. Adv.* **2017**, *3*, eaao5616.
[33] E. Aydin, T. G. Allen, M. De Bastiani, L. Xu, J. Ávila, M. Salvador, E. Van Kerschaver, S. De Wolf, *Nat. Energy* **2020**, *5*, 851.
[34] L. Hong, J. V. Milic, P. Ahlawat, M. Mladenovic, D. J. Kubicki, F. Jahanabkhshi, D. Ren, M. C. Gelvez-Rueda, M. A. Ruiz-Preciado, A. Ummadisingu, Y. Liu, C. Tian, L. Pan, S. M. Zakeeruddin, A. Hagfeldt, F. C. Grozema, U. Rothlisberger, L. Emsley, H. Han, M. Graetzel, *Angew. Chem.* **2020**, *59*, 4691.
[35] R. Wang, J. Xue, K. L. Wang, Z. K. Wang, Y. Luo, D. Fenning, G. Xu, S. Nuryyeva, T. Huang, Y. Zhao, J. L. Yang, J. Zhu, M. Wang, S. Tan, I. Yavuz, K. N. Houk, Y. Yang, *Science* **2019**, *366*, 1509.
[36] R. Szostak, J. C. Silva, S.-H. Turren-Cruz, M. M. Soares, R. O. Freitas, A. Hagfeldt, H. C. N. Tolentino, A. F. Nogueira, *Sci. Adv.* **2019**, *5*, eaaw6619.
[37] M. Liu, A. Barth, *J. Biol. Chem.* **2004**, *279*, 49902.
[38] N. Li, Y. Luo, Z. Chen, X. Niu, X. Zhang, J. Lu, R. Kumar, J. Jiang, H. Liu, X. Guo, B. Lai, G. Brocks, Q. Chen, S. Tao, D. P. Fenning, H. Zhou, *Joule* **2020**, *4*, 1743.
[39] E. T. Hoke, D. J. Slotcavage, E. R. Dohner, A. R. Bowring, H. I. Karunadasa, M. D. McGehee, *Chem. Sci.* **2015**, *6*, 613.
[40] Q. Du, C. Zhu, Z. Yin, G. Na, C. Cheng, Y. Han, N. Liu, X. Niu, H. Zhou, H. Chen, L. Zhang, S. Jin, Q. Chen, *ACS Nano* **2020**, *14*, 5806.
[41] G. Kim, H. Min, K. S. Lee, D. Y. Lee, S. M. Yoon, S. I. Seok, *Science* **2020**, *370*, 108.
[42] N. Yang, C. Zhu, Y. Chen, H. Zai, C. Wang, X. Wang, H. Wang, S. Ma, Z. Gao, X. Wang, J. Hong, Y. Bai, H. Zhou, B.-B. Cui, Q. Chen, *Energy Environ. Sci.* **2020**, *13*, 4344.
[43] H. Zhang, X. Fu, Y. Tang, H. Wang, C. Zhang, W. W. Yu, X. Wang, Y. Zhang, M. Xiao, *Nat. Commun.* **2019**, *10*, 1088.
[44] L. Liu, J. Lu, H. Wang, Z. Cui, G. Giorgi, Y. Bai, Q. Chen, *Mater. Rep., Energy* **2021**, *1*, 100064.
[45] L. Wang, H. Zhou, N. Li, Y. Zhang, L. Chen, X. Ke, Z. Chen, Z. Wang, M. Sui, Y. Chen, Y. Huang, L. Li, Z. Xu, Q. Chen, L.-D. Sun, C.-H. Yan, *J. Mater. Chem. A* **2020**, *8*, 14106.